The Thesis Committee for Tyler Watts
Certifies that this is the approved version of the following Thesis:

Design and Optimization of a Long Travel, Two-Axis Flexural Nanopositioning Stage

APPROVED BY
SUPERVISING COMMITTEE:

Michael Cullinan, Supervisor

Wei Li

Design and Optimization of a Long Travel, Two-Axis Flexural Nanopositioning Stage

by

Tyler Watts

Thesis

Presented to the Faculty of the Graduate School of

The University of Texas at Austin

in Partial Fulfillment

of the Requirements

for the Degree of

Master of Science in Engineering

The University of Texas at Austin

May 2024

Acknowledgements

I would like to extend my deepest gratitude to Dr. Michael Cullinan, whose support, insightful guidance, and encouragement has been invaluable throughout the entire process of this thesis. His expertise and mentorship have truly shaped the outcome of this work. I am also immensely grateful to Dr. Wei Li for graciously serving as the reader for this thesis and providing valuable feedback and suggestions. I would also like to give a special thanks to Sridharan Vasu for his prior research and guidance with my project. And to my parents, whose endless love, encouragement, and sacrifices have been the foundation of my academic journey, I owe an immense debt of gratitude; without your support, I would not have achieved any of my goals.

Abstract

Design and Optimization of a Long Travel, Two-Axis Flexural Nanopositioning Stage

Tyler Watts, M. S. E.

The University of Texas at Austin, 2024

Supervisor: Michael A. Cullinan

This thesis details the design, computational optimization, and resultant evaluation of a two-axis flexural nanopositioning stage based on a modified version of a double parallelogram flexure which features underconstraint-eliminating features nested within the flexural bearing. The stage was optimized using a response surface model with the seven most sensitive geometric parameters for the flexural bearing as inputs, and the flexure's peak stress and reaction force at maximum deflection as outputs. This paper shows that—through design optimization—the first resonant mode of a long travel, two-axis flexural nanopositioning stage that has previously been reported in literature can be improved by a factor of two while still maintaining the higher-order resonant modes to be at least an order-of-magnitude higher than the fundamental mode of the stage. This improvement is critical because increasing the fundamental mode without sacrificing the higher order modes will allow for a higher bandwidth controller to be implemented on this nanopositioning stage. The end goal of the positioning stage detailed in this paper is to be implemented within a micro-SLS 3D printer.

Table of Contents

List of Tables

List of Figures

Chapter 1: Introduction

The purpose of this research is to improve the design of the long travel flexural bearing nanopositioning stage which was developed by [13] and subsequently improved by [15]. This paper presents a detailed description of the design process for a long travel flexure-based precision nanopositioning stage with a focus on the optimizing the flexure building blocks of the stage for maximum dynamic performance in the end use case of the stage.

1.1) Background and Motivation

Multi-axis positioning stages with nanometer accuracy and long travel are highly desirable in the field of precision engineering due to the large number of applications which require object positioning with precision orders of magnitude smaller than the range of stage operation. For example, scanning electron microscopes (SEM), atomic force microscopes (AFM), semiconductor manufacturing, micro-additive manufacturing (micro-AM), micro-assembly, and micro electrical mechanical systems (MEMS) manufacturing require positioning stages with nanometer-accuracy and a high degree of repeatability over a long range [8] [14] [21] [17]. The most prevalent positioning stages for these high precision, long travel applications within industry settings are typically magnetic levitation or air bearing based designs [6], but flexural bearing stages are a popular alternative due to their low cost and high degree of customizability for the application at hand.

Flexure-based positioning stages are commonly used for high precision, small stroke applications, but they are much less common when both high precision and long

stroke are required. Currently, many high precision, long stroke positioning needs are addressed with multibody positioning stages driven by precision actuators, but the complex nature of multibody precision positioning stages and their required maintenance raises the operating costs for these processes. Traditional multibody positioning stages are often contact based designs which use electronic actuators to generate motion through lead screws, ball screws, or rack and pinion drives and guide the stage with planar or rotary bearings. All of the aforementioned mechanical elements are subject to friction and backlash which hinder sub-micron accuracy and require complex control systems to maintain high positioning accuracy. If sub-micron precision is required, these stages are often paired with a high precision, short stroke flexural stage which is coupled to the long stroke multibody stage. The advantage that flexural bearing stages have over traditional multibody positioning stages is the elimination of friction and backlash, which—when paired with a precision actuator—can allow for nanopositioning for a fraction of the cost of more expensive systems used in industry [18]. Thus, the development of flexural positioning stages which are both high precision and long stroke is important to the continuation of research within many fields of precision engineering.

In recent years, there has been further development into flexural positioning stages that offer high precision and long stroke with improved dynamic performance due to new innovations in flexure bearing design [5]. In their 2018 study, Roy and Cullinan successfully fabricated a novel long-travel nanopositioning stage based on compliant mechanisms which was designed for use within their micro selective laser sintering (uSLS) 3D printer prototype [13]. This work was notable because it dramatically expanded the

typical travel limits of flexural positioning stages which are usually in the sub-centimeter range at most. Not only was this stage a dramatic improvement in flexural positioning stage travel limits, but by using a modified flexure design from [11], Roy and Cullinan were also able to increase the dynamic performance of their stage with a second revision design that has promising improvements over classic flexural stages. Improving dynamic performance for the flexural positioning stages can have far reaching impacts within the field of precision manufacturing. For example, stages which can move quicker and travel further while maintaining high precision can allow higher throughput in MEMS manufacturing, which can help lower the cost of electronic components that are now daily use items for many people around the world. Within the field of microscopy and part analysis, the cost of outsourcing the use of any high-resolution microscope can be reduced if the machine can operate faster with improved positioning stage performance from a flexural stage rather than a multibody stage. This would make the use of SEM and AFM analysis cheaper, giving researchers more access to these technologies for a wide range of studies.

Despite the aforementioned advantages that flexure-based positioning stages have over their rigid body counterparts, this type of positioner also has many drawbacks. As previously stated, flexural positioning stages with nanometer accuracy are typically limited to small overall travel limits of around 1mm per axis, with the longest travel stages usually not exceeding 10mm per axis [10]. This severely limits the usability of the precision stages and often results in flexural positioning stages being paired with a traditional multibody positioner to handle coarse, long travel movements [16]. Another drawback is that the ratio

of the footprint of flexural stages relative to their travel limits—referred to as their "area ratio"—is often very large due to the nature of current flexural bearing designs. This large area ratio makes flexural stages difficult to package in tight spaces within existing machinery, but researchers in recent years have made many improvements in flexure bearing designs intended to reduce the area ratio [16] [10]. Additionally, because these stages are often comprised of long, thin flexural beams which are purposefully compliant, they frequently have low first resonance frequencies and suffer from limited dynamic operating speeds. Because this limitation on dynamic performance is an issue in many potential applications of flexural positioning stages, significant research has been conducted to mitigate this problem.

This paper details the redesign, simulation, optimization, and testing of a new long-travel flexural XY positioning stage for the uSLS printer developed by [13] with a focus on improving dynamic performance over previous designs. Positioning stage performance will be evaluated by the following criteria: motion range, linear stiffness, natural frequency, life estimate of complaint stage, and overall stage footprint. The evaluation criteria are detailed below in Table 1. Designing a positioning stage which meets or exceeds the outlined criteria will improve the performance of the uSLS printer—the machine which this stage will ultimately operate within—by allowing for faster printing, ensuring print dimensional/repeatability issues do not stem from the nanopositioning stage, and reducing the frequency of component replacement due to fatigue. Additionally, the successful achievement of the targets listed below will further contribute to the knowledge base of

design techniques for flexural positioning stages and create more potential use cases for this affordable, precise positioning technology.

Evaluation Criteria	**Target Value**
Motion range of stage center	50mm x 50mm
Linear stiffness of a single axis	1.44 N/mm maximum (actuator limited)
First natural frequency modes of full stage	As high as possible with stiffness limitations
Fatigue life estimate	Greater than or equal to 10^9 cycles
Stage planar footprint	600mm x 600mm or smaller

Table 1: Outline of design requirements

Chapter 2: Stage Design

2.1) Flexure Selection

The design of the nanopositioning stage began with the selection of which flexure bearings should serve as the basis for the motion of the stage. When selecting flexures for use in a precision motion application, researchers typically either select a flexure bearing which has been designed for a specific type of motion (e.g. prismatic or rotary flexures) or create their own design based on documented flexural building blocks such as circular flexural hinges or leaf hinges [3]. For applications which require linear motion, the most popular predesigned flexure geometry is the double parallelogram flexure (DPF)—shown in Figure 1—because of its highly linear deflection behavior which stems from its nested parallelogram layout that eliminates the majority of nonlinear motion during deflection. The DPF now has many offshoot variants due to its popularity which has led to a stream of design improvements and alternative designs based on the DPF platform in recent years. On the other hand, custom flexure bearing designs are also extremely popular for multi-axis motion applications. For example, Qin et al. [12] described the design and analysis process for a statically indeterminate flexure structure in their 2012 paper which shows how translational and rotational movement can be achieved by careful placement of flexural notch hinges. The researchers were able to design flexures with motion across multiple axes which were very stiff in all non-motion directions and showcased the careful use of over constraint as a stiffening method for flexure bearings [12]. These designs were achieved solely through the use of flexural notch hinges, and the use of notch hinges with more complicated profiles such as elliptical or parabolic cutouts has only grown since that

paper's publication. Some researchers have also proposed the use of 3D revolute notches which would allow out of plane rotation to be easily incorporated into a chain of notch flexures, further expanding the ever-growing list of flexural building blocks [3]. These methods of custom flexure design are attractive since they allow conventional rigid body linkage designs to be adapted into a complaint design which eases the ideation process for mechanism synthesis. For example, the nanopositioning system developed by Lee et al. in their 2017 publication made use of guiding flexures which were a compliant variant of a four-bar linkage created using notch flexures as rotary joints [9].

For the application at hand, however, a predesigned flexure bearing was preferred due to the large stroke length required in the uSLS printer. In their previous designs for long travel nanopositioning stages, Roy & Cullinan and Thirumali [13] [15] made use of a custom variant of the DPF platform pioneered by [11] which dramatically improved the dynamic performance of the flexure bearing by adding an underconstraint elimination feature nested within the flexure's footprint. In recent years, however, research into alternatives to the DPF have been proposed by Lyu et al. and Xu [10] [16] in which additional parallelogram flexures have been nested within the DPF to create a multi-stage parallelogram flexural bearing (MCPFs) to reduce the footprint of the DPF without compromising its deflection capabilities. MCPFs present a significant advantage over traditional DPFs because they can be used to create a more compact flexural positioning stage with a higher area ratio—the ratio of the usable travel range of the positioning stage to the stage's 2D area. Increasing the area ratio of flexural positioning stages is an important goal for integrating designs within larger machines where packaging is a

concern. In the case of the uSLS machine, however, stage footprint reduction is not required due to the large, open nature of the machine which was originally designed for use with a DPF-based stage with a low area ratio. Additionally, MCPFs suffer from poor resonance behavior when compared with optimized DPF variants. Because the DPF architecture only has two movement stages, past work from [11] has presented a modified DPF design which incorporates an additional linkage packaged within the intermediate and final stages of the DPF to eliminate the inherent underconstraint between them. The underconstraint-eliminating DPF (UEDPF) has been shown to have significant dynamic performance increases over the classic DPF design, and the most sensitive parameters for the flexure have already been identified for ease of optimization in other applications. Figure 1 below shows the differences in geometry between the DPF and UEDPF architecture in both static and deformed states. MCPFs show promise for reducing the area ratio of compliant positioning systems, but they present a significant challenge in terms of underconstraint elimination due to the presence of more than two nested stages which makes a planar underconstraint elimination solution difficult. Thus, the flexure bearing design selected for use on this positioning stage is the UEDPF proposed by [11].

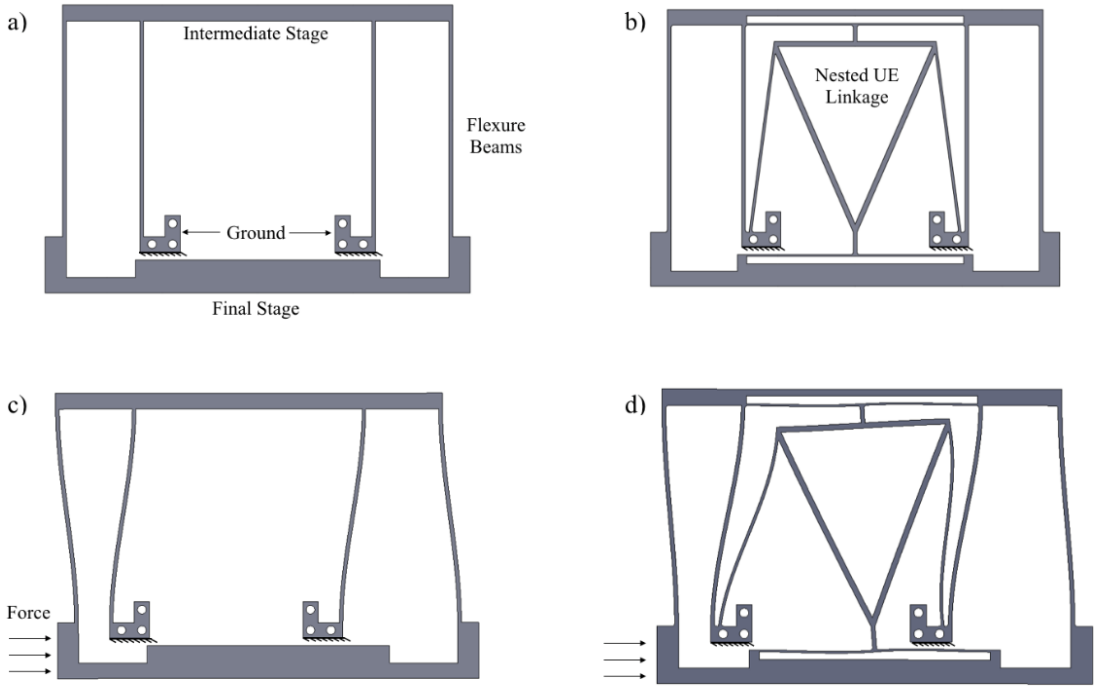

Figure 1: a) Static DPF b) Static UEDPF c) Deformed DPF d) Deformed UEDPF

2.2) HIGH-LEVEL STAGE ARCHITECTURE

For multi-axis positioning stages, the high-level stage architecture is critical to achieving an optimized footprint and expanding the working bandwidth of the positioner. For two-axis positioning, there are two broad types of stage layouts: serial and parallel. In a serial configuration, one actuator will remain fixed while the other will travel with the movement of the first axis. In a parallel configuration, both actuators remain fixed and only the stage itself moves. Serial stages have the capability to easily decouple movement between the two axes and can achieve high dynamic performance when only the secondary axis is in use [18], but they often suffer from poor dynamic performance on the primary axis due to the added mass of the secondary's axis' actuator. For all long-travel

applications, actuators tend to be orders of magnitude heavier than the flexural bearings they displace, so a serial stage architecture was not chosen for this nanopositioning stage. Parallel stages, on the other hand, have lower potential for dynamic performance, but their performance is often nearly identical in both axes. They often suffer from more motion coupling between axis than their serial counterparts, but with a position sensor on both axes, a control system can be used to reduce this crosstalk to manageable values [16]. Parallel stages themselves have two broad categories: planar or stacked. The planar configuration can be easily monolithically fabricated, but the stage's footprint is usually significantly larger than that of an equivalent vertically stacked stage. For these reasons, a vertically stacked parallel stage was chosen for the layout of this nanopositioner. Figure 2 below shows the difference between parallel and serial stage layouts while Figure 3 shows an exploded assembly of the final stage design for this paper.

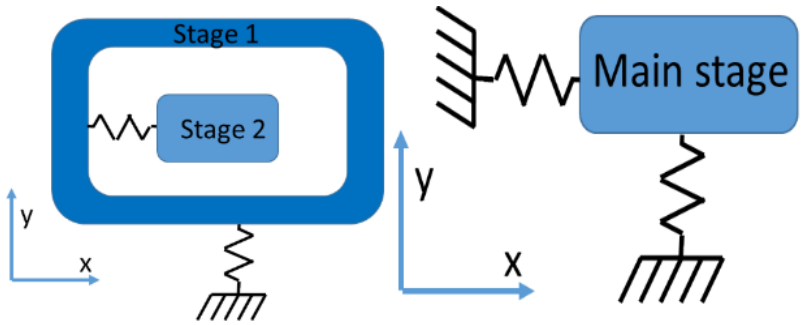

Figure 2: Serial (left) vs. parallel (right) stage layouts

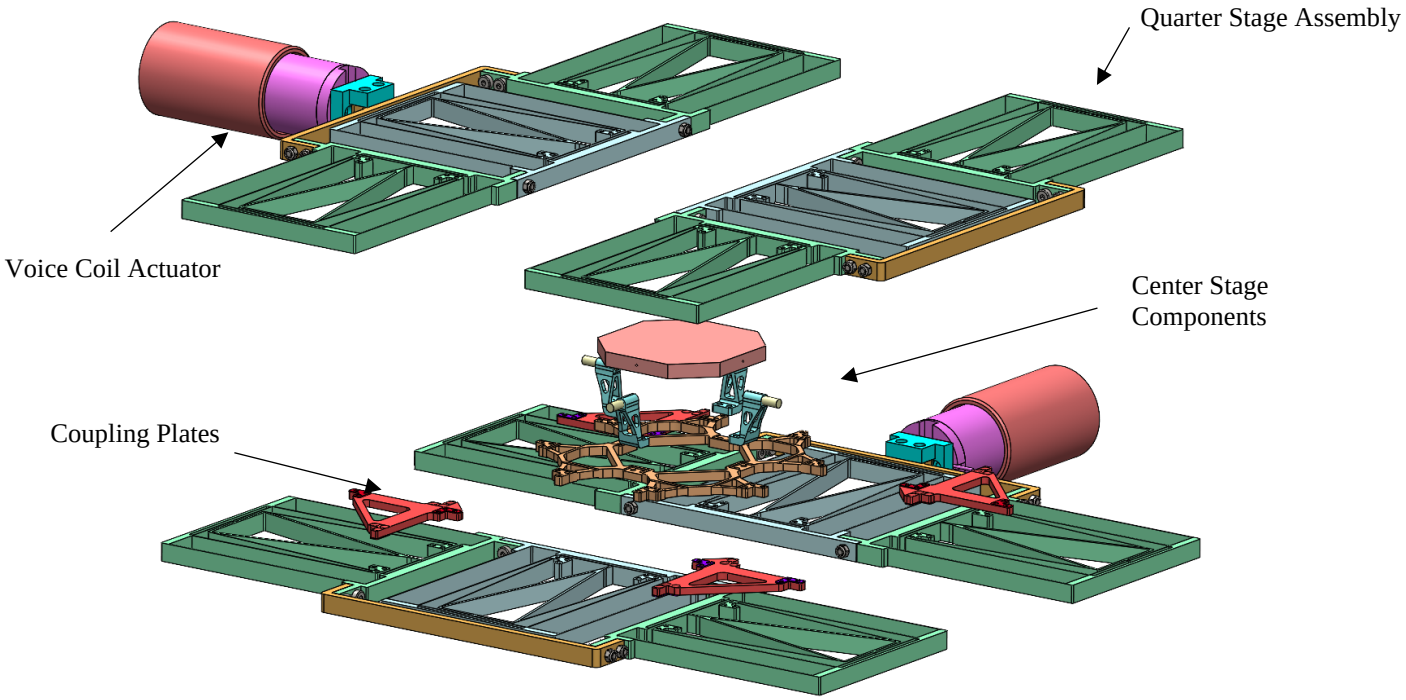

Figure 3: Exploded assembly of new stage design

Another component of the high-level stage architecture which must be addressed is the manufacturability considerations of the compliant positioning stage. Because the baseline stage was fabricated monolithically via waterjet cutting, there were significant deviations from nominal dimensions in the final product due to the fidelity of the chosen manufacturing method [13]. The waterjet cutting of 0.5" thick Aluminum 7075 plate resulted in tapered cuts which had a significant effect on the final stiffness and behavior of the positioning stage. As a result, the method of manufacturing for this stage design was reconsidered before optimization began. For the fabrication of planar compliant mechanisms such as DPFs or MCPFs, the most common methods used are waterjet cutting and wire EDM cutting. Traditional milling methods can be used to fabricate flexures [5],

but the geometries which can be achieved via milling are limited and the component scrap rate is high so it was not selected as a viable method for the stage fabrication. Due to the significant precision increase that wire EDM has over waterjet cutting, wire EDM was chosen as the manufacturing method for this positioning stage. Due to limitations on working area size of the wire EDM machine used for fabrication, each mirrored "quarter stage" had to be split into four separate pieces and coupled via fasteners, creating a quarter stage assembly (QSA) which serves as the building blocks for the stage. Figure 4 below shows an exploded view of a QSA. The quarter stage was split to ensure manufacturability even as flexure sizes changed and to allow maximum modularity in the event that flexures ever need to be swapped out due to damage or upgrades.

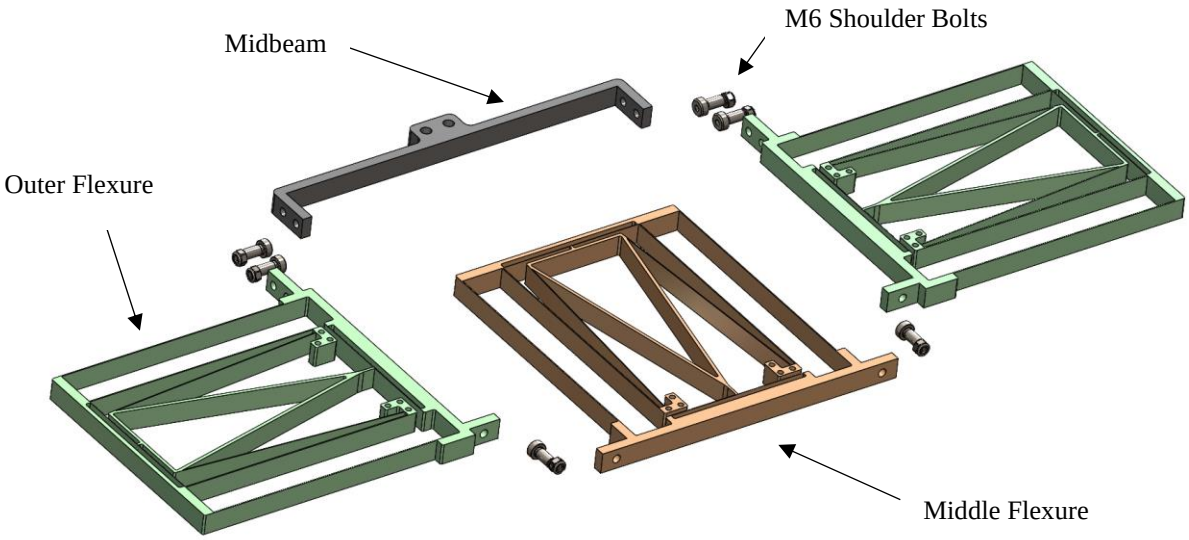

Figure 4: Exploded assembly of a quarter stage assembly (QSA)

For the coupling of the quarter stage assembly, fastener selection and placement was considered carefully. Precision M6 shoulder bolts were chosen for the coupling

fasteners because their precision-ground shoulder was used to create a slip-fit on reamed holes in the flexures and ensure full assembly fidelity. Each bolt is paired with a low-profile nylon insert locknut to ensure the fasteners do not loosen during stage operation. The chosen locations for the fasteners lie on the outside of each UEDPF flexure, in an area where no elastic deformation of the stage will cause an interference between a fastener and a flexure beam. Additionally, the selected locations allow the maximum amount of access for assembly and disassembly of the stage using hex keys and standard spanner wrenches.

2.3) Actuator Considerations and Selection

The range, speed, and dynamic performance of precision nanopositioning stages is heavily dependent on the actuators used to drive the positioning stage. Because extremely high precision is required, the types of actuators commonly used on compliant positioning stages are usually limited to shape memory alloy actuators (SMAs), magnetostrictive actuators (MSAs), piezoelectric actuators (PAs), and electromagnetic actuators such as voice coil actuators (VCAs) or magnetic levitation actuators (MLAs). The long travel nature of this positioning stage limits actuator options even further with 50mm stroke and nanometer precision required. Though the use of short-stroke PAs and MSAs can be amplified through flexural amplifiers to provide long-range motion [17], the stroke length and actuation force required in this application is large enough that an amplifier with a piezoelectric or magnetostrictive actuator would not be sufficient. Thus, the actuators left to select from are the electromagnetic actuators: VCAs and MLAs. Due to the price and

implementation costs of MLAs, a voice coil actuator was selected for use with this positioning stage.

For the selection of a VCA, the most important parameters are stroke length, dynamic mass, peak actuation force, and overall size. VCAs come in two common configurations: moving coil or moving magnet. Because dynamic mass needs to be minimized, only moving coil options were considered since their dynamic mass to peak force ratio was far higher than the moving magnet options. After examining a wide range of moving coil VCAs which met the stoke length requirement, the chosen VCA for the application was H2W Technologies NCC34-25-060-1X model which has a peak actuation force of 38.7N at 100% duty and a stroke of 85mm [4]. Thus, the stiffness of the flexures can be optimized to work within the bounds of the chosen actuator.

2.4) NON-FLEXURAL COMPONENTS

In most flexural positioning stage designs—including this one—one of the main goals is to achieve as wide a dynamic performance bandwidth as possible by pushing out the resonant modes of the stage. Because resonant modes are dependent on geometry, stiffness, and mass, the focus of many papers on this topic revolves around optimizing the flexures for maximum stiffness within the constraints of selected actuators and travel requirements, but mass reduction as a means of achieving dynamic performance increase is rarely employed. Therefore, during the design process for this positioning stage, a focus on using the non-flexural parts of the stage to increase the performance of the assembly was employed to further benefit the flexural optimization's performance increases.

At the center of the nano-positioning stage lies several non-flexural parts which hold the stage together and support the sample holder for printing. These components carry significantly more mass than the flexures and are coupled to the actuators through the UEDPF flexures, causing the system to behave similarly to an undamped mass-spring system during rapid actuation of the stage. Additionally, the large mass at the center of the stage lowers the maximum movement speed of the stage due to the inertia of the centralized mass. Thus, an effort was made to redesign the non-flexural parts of the stage to reduce mass as much as possible while maintaining stiffness in all necessary directions.

The first step in reducing the sprung mass of the center stage components is reducing the components to their core functions and combining or eliminating parts wherever possible. The center of the baseline stage consists of three parts: a center plate which holds the flexures together, a sample holder which supports the printing substrate, and an insulation layer which keeps stage temperatures in check from the heat input of the sintering laser. Thus, the only functions of the center stage parts are to act as structural supports for the flexures, to support the printing substrate, and to perform thermal management during the printing process by preventing excessive conduction into the flexures. Using resultant force values from FEA simulations of the flexures discussed later in this paper, structural optimization on the aforementioned components was performed. The newly designed stage center consists of a center plate for coupling the flexural assemblies together and four individual substrate supports which hold the printing platform above the stage. Table 2 below shows the relative mass reduction for each component.

	Center Plate	Substrate Support
Baseline Stage Mass	321g	281g
New Design Mass	102g	35g
Percent Reduction	68.2%	87.5%

Table 2: Mass comparison between baseline stage and new stage center components

Because the baseline stage has been used on the uSLS machine for several years now, thermal data collected from printing was used to justify the elimination of the insulation layer in favor of the new substrate support design which instead provides an increased area for free conduction under the printing substrate. The total mass of the center stage components decreased 77% overall, falling from 602g to 137g. Figure 5 below shows an exploded assembly of the baseline stage's center components while Figure 6 shows the center components designed for the new stage. The modal implications of this mass reduction will be discussed in a subsequent section of this paper.

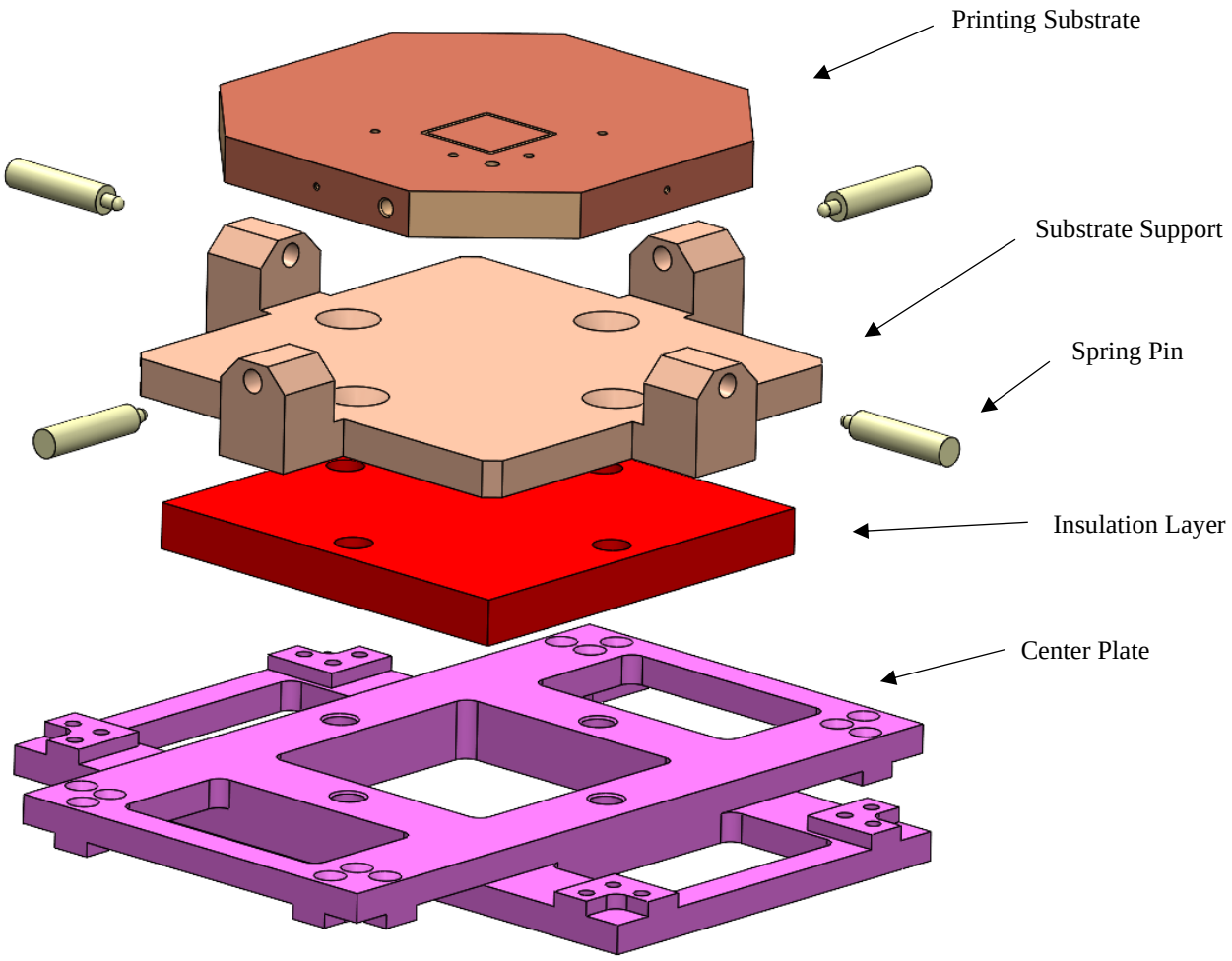

Figure 5: Baseline stage center components

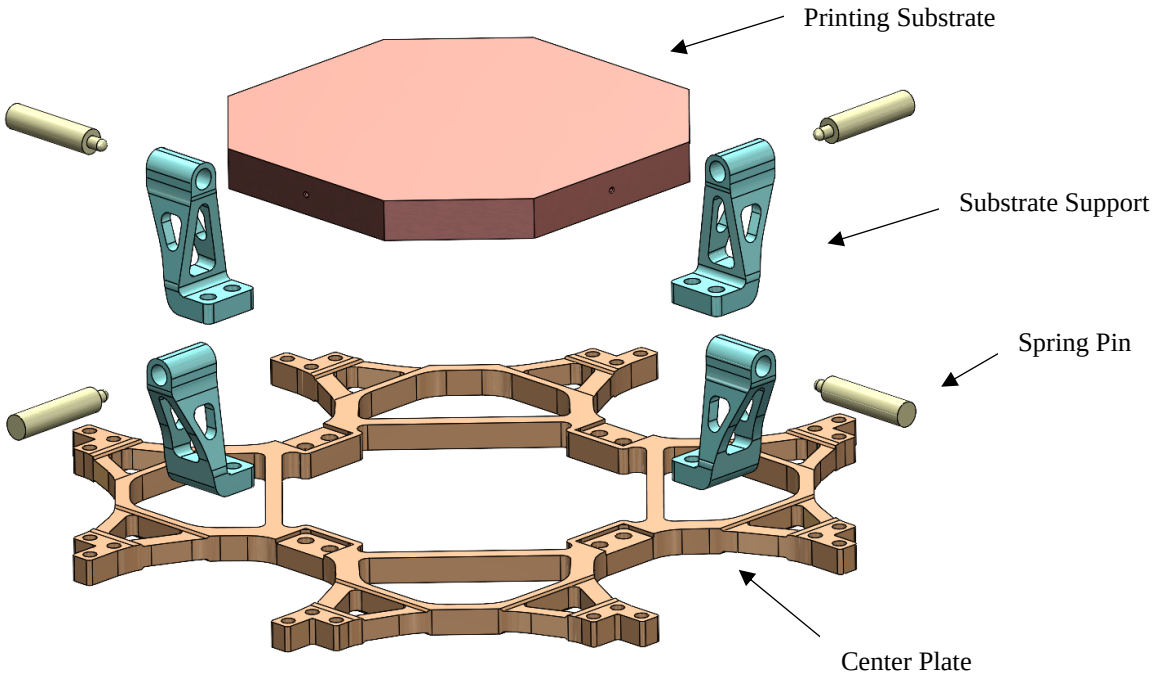

Figure 6: New stage design center components

Chapter 3: Simulation and Optimization

3.1) WORKFLOW

The next step in the stage design process was the optimization of the selected flexures for maximum stiffness within actuator force output limits and stage fatigue life goals. Complaint mechanisms are notoriously more difficult to analyze and characterize motion compared to their rigid body analogues due to their often-nonlinear stiffness behavior and complex motion profiles. Researchers have proposed many methods for complaint mechanism synthesis and analysis such as the pseudo-rigid body method [7], but many of these classic methods lose accuracy as deflections become increasingly large [2]. Modern methods such as the elliptical integral solution [20] show promising results in predicting flexure beam motion and force reaction for a variety of cases, but still present significant challenges when setting up models for more complicated compliant mechanisms such as the UEDPF with its integrated underconstraint elimination features. Additionally, dynamic modeling of flexures with analytical methods requires a separate model which also would require development for the complex profile of the UEDPF flexure [1]. For most flexure optimizations, a basic approach is taken for stiffness modeling with an analytical model, but the final designs are typically validated with FEA and then again with a prototype model for empirical testing. Because of the complexity of the UEDPF's geometry and the previous work of [11] which identified the most sensitive parameters of the UEDPF, FEA will be exclusively used for the analysis and optimization of flexure performance for this stage. Figure 7 below shows the seven most sensitive parameters of the UEDPF which will be used for optimization.

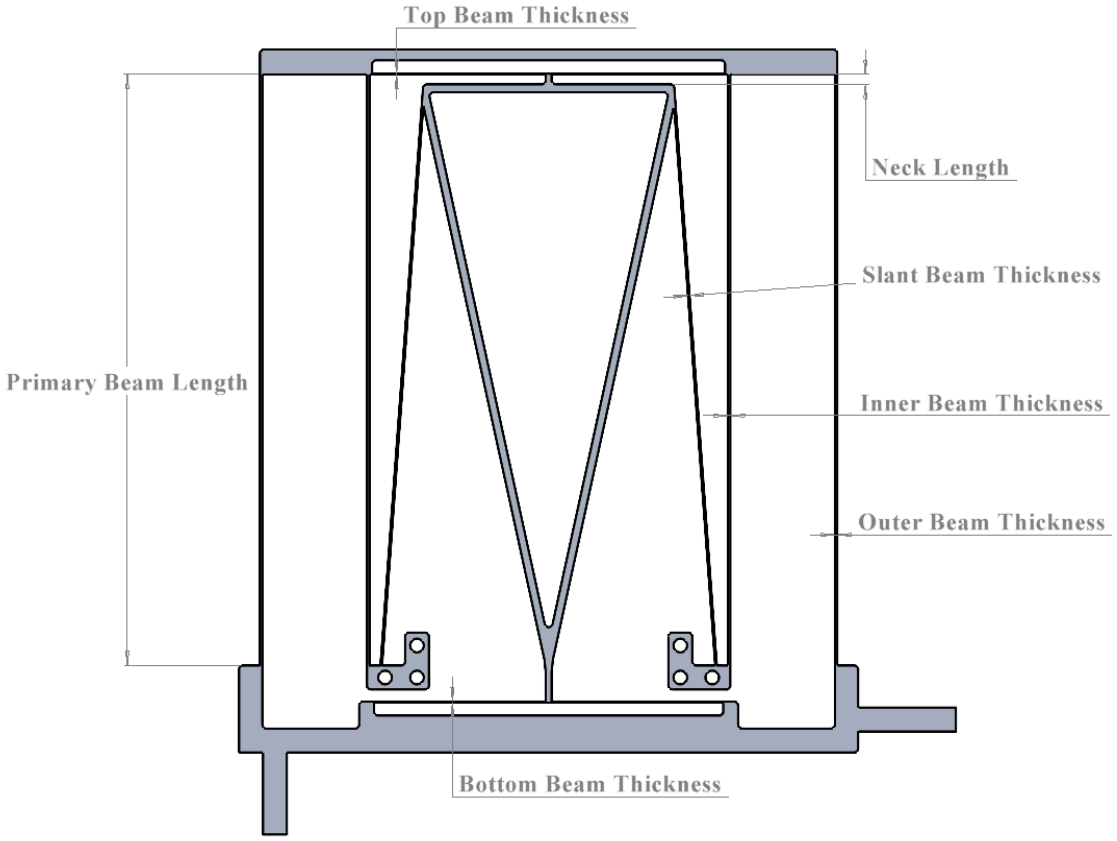

Figure 7: Most sensitive parameters of the UEDPF [11]

Because the FEA simulation of UEDPF flexures is a computationally intensive task, optimizing via FEA data alone is not a valid method of flexure design. Instead, building on the work of [15], the process was divided into the workflow outlined below for the optimization of the UEDPFs used for the nanopositioning stage.

1. 2D FEA simulations of QSAs, run in batches
2. Optimization with ANSYS optimization using the data from the QSA 2D FEA to train a response surface model
    a. Identification of ideal candidate points
    b. Verification of candidate points and model fidelity using 2D FEA
3. Verification of the chosen parameters with a 3D FEA of a QSA
4. Full stage 3D FEA simulations of final flexure designs

Instead of directly simulating a large number of flexure configurations, parameter ranges for the seven most sensitive dimensions of the UEDPF identified in [11] are defined and 2D FEA simulations of various parameter sets are run in batches. The data from the batch runs is used to train a response surface model in ANSYS to predict 2D FEA results for input parameters sets to avoid the high computational costs of FEA simulations. The ANSYS optimization tool is then used in conjunction with the trained response surface model to optimize the QSAs for target values. The candidate points generated from the ANSYS optimization are then verified with 2D FEA simulations to evaluate the performance of the response surface model at predicting FEA results. If the response surface model was accurate enough and the optimizer converged properly, the input parameter sets for the 2D FEA batch runs were refined around the candidate point and the process was run again to increase the accuracy of the response surface model and obtain the most ideal UEDPF geometry. This process was repeated until 1) the response surface model is sufficiently accurate at predicting 2D FEA results and 2) the optimization's candidate point no longer changed with subsequent iterations. Once this candidate

geometry has been established, a full high-fidelity mesh 3D FEA of a QSA with the candidate point geometry was performed to ensure the 2D FEA properly predicted 3D FEA stiffness and peak stress values. As a final step, a 3D FEA of the full stage with resultant QSAs was performed to validate the modal and mechanical behavior of the stage as a whole. The following chapters of this paper will discuss each step of this process in further detail, and the results from the simulations will be further discussed in the results section of this paper.

3.2) 2D QSA SIMULATIONS

The first step in the simulation and optimization of the stage begins with 2D FEA simulations of QSAs. Despite past research from [15] focusing on 2D FEA simulations of single flexure simulations at first, it was discovered during this design process that simulation of a single flexure can lead to failing designs when the flexure is later fitted in a quarter stage configuration. Because a single flexure's parasitic motion perpendicular to its deflection direction is non-negligible with the large deflections required for this positioning stage, single flexures optimized on their own will oftentimes yield when put in a QSA; the parasitic motion of the two flexures on opposite sides of the QSA will impose perpendicular stress on one another, causing excessive beam deformation and even failure. Thus, the most basic 2D FEA simulations were run with QSAs rather than single flexures.

Table of Design Points

	A	B	C	D	E	F	G	H	I	J	K
1	Name	P1 - Half_OBT	P2 - Half_IBT	P3 - Primary_Beam_Length	P4 - Top_Beam_Thickness	P5 - Bottom_Beam_Thickness	P6 - Slant_Beam_Thickness	P7 - Neck_Length	P8 - Equivalent Stress Maximum	P9 - All - Force Reaction - Fixed Support - End Time Maximum Total	Retain
2	Units	mm	mm	mm	mm	mm	mm	mm	MPa	N	
3	DP 200	0.35	0.3	99.8	0.33	0.4	0.2	2	332.79		☑
4	DP 201 (Current)	0.246	0.549	139.14	0.543	0.503	0.649	4.12	304.18	3.2453	☑
5	DP 202	0.3	0.3	93	0.6	0.6	0.6	2.3	401.6		☑
6	DP 203	0.3	0.3	93	0.6	0.6	0.6	6	0		☑
7	DP 204	0.39	0.36	106.03	0.26	0.45	0.55	2.8	401.6		☑
8	DP 205	0.49	0.4	131.16	0.31	0.42	0.38	3.07	401.6		☑
9	DP 206	0.29	0.37	125.38	0.5	0.57	0.43	2.88	401.6		☑
10	DP 207	0.43	0.35	115.08	0.48	0.38	0.27	5.7	401.6		☑
11	DP 208	0.29	0.29	144.47	0.36	0.33	0.45	4.91	401.6		☑
12	DP 209	0.25	0.37	111.06	0.42	0.33	0.37	3.53	401.6		☑
13	DP 210	0.49	0.26	142.96	0.38	0.31	0.52	5.72	529.47		☑
14	DP 211	0.41	0.24	106.28	0.25	0.56	0.26	4.09	401.6		☑
15	DP 212	0.5	0.2	124.37	0.37	0.58	0.26	5.74	401.6		☑
16	DP 213	0.5	0.2	124.37	0.37	0.58	0.26	5.74	529.47		☑
17	DP 214	0.38	0.24	143.72	0.38	0.54	0.24	2.74	401.6		☑
18	DP 215	0.29	0.34	124.12	0.48	0.39	0.25	4.61	601.07		☑
19	DP 216	0.37	0.2	146.73	0.37	0.28	0.53	5.64	401.6		☑
20	DP 217	0.26	0.45	114.07	0.44	0.5	0.24	3.37	401.6		☑
21	DP 218	0.31	0.37	141.96	0.25	0.28	0.37	5.6	401.6		☑
22	DP 219	0.39	0.28	116.83	0.43	0.58	0.36	5.88	401.6		☑
23	DP 220	0.44	0.21	142.71	0.34	0.3	0.38	3.75	401.6		☑
24	DP 221	0.47	0.5	126.38	0.24	0.48	0.46	4.05	401.6		☑
25	DP 222	0.4	0.21	105.78	0.31	0.49	0.23	5.02	401.6		☑
26	DP 223	0.49	0.42	141.46	0.53	0.34	0.22	4.55	401.6		☑
27	DP 224	0.4	0.22	103.52	0.46	0.42	0.45	5.46	401.6		☑
28	DP 225	0.37	0.38	108.04	0.42	0.39	0.24	2.06	401.6		☑
29	DP 226	0.41	0.42	122.11	0.42	0.35	0.32	5.2	401.6		☑
30	DP 227	0.34	0.34	148.49	0.36	0.21	0.59	5.18	401.6		☑
31	DP 228	0.5	0.25	100.5	0.46	0.4	0.29	3.71	401.6		☑
32	DP 229	0.41	0.23	129.65	0.45	0.21	0.52	4.99	401.6		☑
33	DP 230	0.2	0.36	130.15	0.41	0.33	0.22	4.71	401.6		☑
34	DP 231	0.26	0.44	139.7	0.43	0.26	0.31	2.76	401.6		☑
35	DP 232	0.3	0.28	127.64	0.56	0.31	0.3	3.49	401.6		☑
36	DP 233	0.3	0.39	108.29	0.35	0.53	0.31	3.99	401.6		☑
37	DP 234	0.26	0.35	132.16	0.37	0.46	0.27	5.36	401.6		☑
38	DP 235	0.48	0.49	147.24	0.39	0.41	0.39	6	401.6		☑
39	DP 236	0.24	0.33	113.83	0.33	0.47	0.47	5.52	401.6		☑

Figure 8: Example parametric table for 2D FEA runs

Because the 2D FEA simulations were run in batches, proper FEA setup was critical to obtaining results and preventing simulation crashes. The geometry was sketched in ANSYS DesignModeler to allow for parametric geometry definition within ANSYS Workbench. Figure 8 above shows a part of a parameter table from a 2D FEA batch run. The 2D FEA used planar 2D elements with a plane stress condition to evaluate the performance of the model. In the interest of saving computational time, the middle flexure was omitted from the QSA model for this step since it was not deformed. The simulation applied fixed constraint boundary conditions to the two faces of the grounded stage and a displacement boundary condition of 25mm to the VCA coupling face. The meshing method for these simulations was ANSYS' triangular mesh since it had the least errors generating over a wide variety of parametrically-modeled 2D geometries. The mesh size

was split by faces on the QSA; the rigid parts of the QSA were modeled with a mesh element size of 0.5mm while the flexure beams used 0.1mm elements and the top & bottom beams of the underconstraint elimination geometry used 0.05mm elements. Figure 9 below shows a close up view of the mesh used on the 2D simulations, and Figure 10 below that shows the boundary condition setup for the simulations.

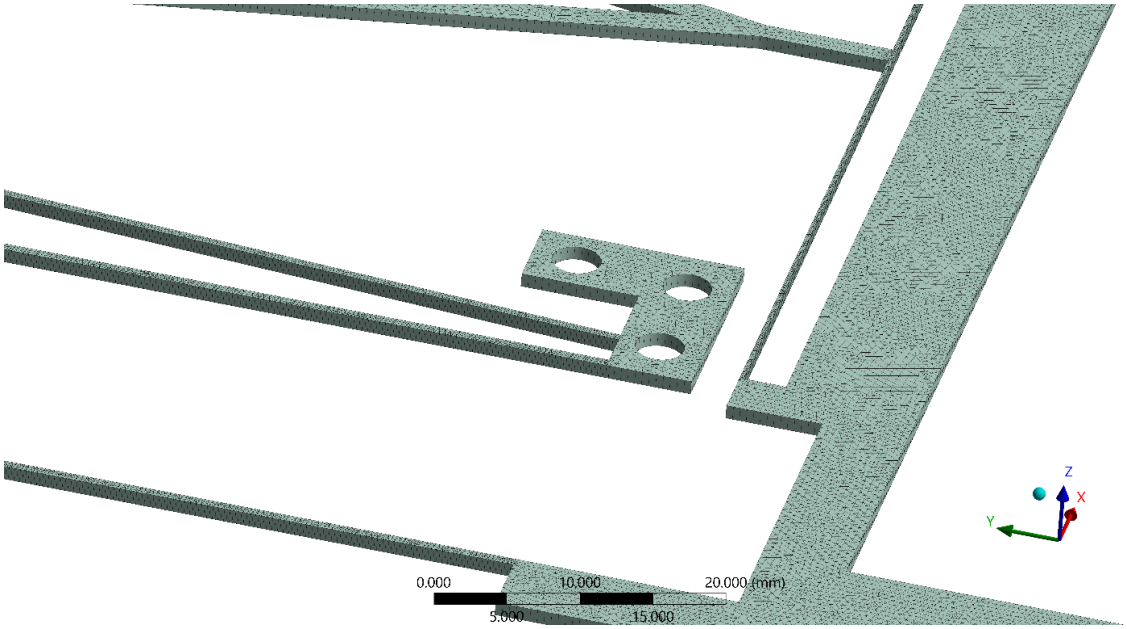

Figure 9: Close up view of the mesh for the 2D FEA simulations

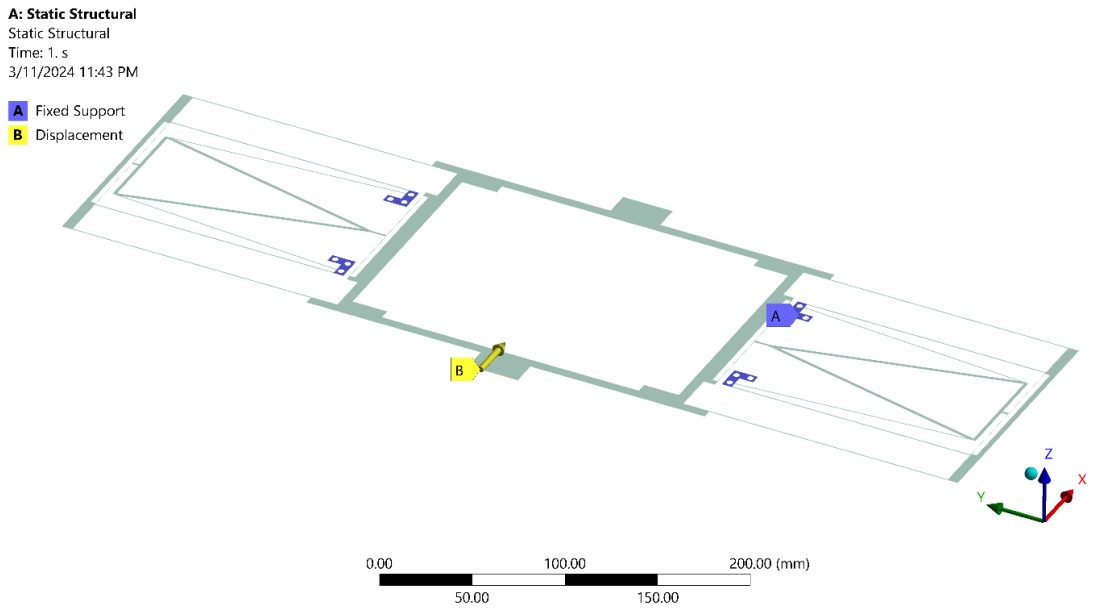

Figure 10: Boundary condition setup for the 2D FEA simulations

Parameter sets were then generated using PyDOE, a Python package which facilitates the creation of DOE matrices with given input parameter ranges. It was experimentally determined that batches of 200 simulations at a time with the given setup and computational power available would yield results in a meaningful time, so all simulation batch runs were done in sets of 200. The input parameter range was kept as wide as possible for the first batch of simulations so no potential candidate point would be ignored. As subsequent simulations were run, the input parameter ranges fed into PyDOE were refined to reflect the trends of the optimization results in an effort to refine the response surface model within the range of the candidate point. Once suitable data was generated from the 2D FEA, it was fed into the response surface model discussed in the

next section of this paper. Figure 11 below shows an example result of a 2D FEA simulation.

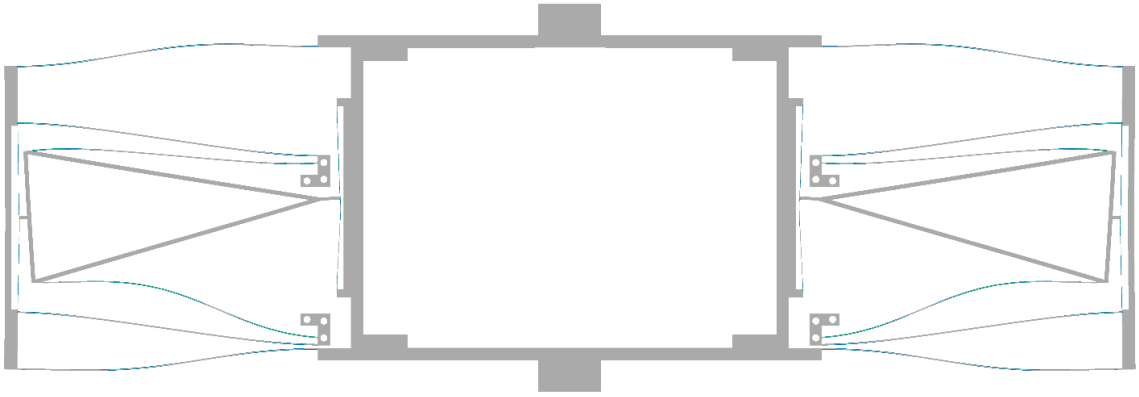

Figure 11: Example result from a 2D FEA simulation of a QSA

3.3) Response Surface and Optimization

The next step of the design process involved training a response surface model from the results of the 2D FEA batch runs and using that model in conjunction with ANSYS optimization to generate candidate parameter sets for further evaluation. In [15], the researcher used a custom genetic algorithm and neural network coded in MATLAB to perform the modeling and optimization steps, but ANSYS response surface optimization was chosen instead for this study because of the integration that ANSYS has with the main model. Using ANSYS' built-in response surface optimization allows for automatic model checking by verifying response surface model predicted values with values from new simulation points generated to test key aspects of the response surface model.

The system to be optimized was a seven-input, two-output model. The seven input parameters were the most sensitive parameters for the UEDPF identified by [11], and the

two outputs were the flexure's peak stress at maximum deflection and the force reaction felt by the 25mm displacement boundary condition. These two outputs were deemed most critical since the two most important considerations at this stage in the flexure design process are the fatigue life and the stiffness of the flexure. Since geometrical size constraints can be placed on the flexure during the optimization stage, only the peak stress and force reaction were taken into consideration for the 2D planar modeling.

Because the optimization was based on a 2D FEA of a large deflection flexure, several considerations had to be taken to predict 3D results from the planar simulation. ANSYS 2D FEA models planar geometries with 1mm thick mesh elements, so the force reaction generated in the 2D simulation would be less than that of the 3D part. From the equation for Eulerian beam bending, the thickness out of plane is directly proportional to the deflection distance. Thus, for simulations of a simplified planar model with 1mm thick flexure elements, the resulting stiffness should be 12.7x higher in 3D because the UEDPFs will be fabricated from 12.7mm thick Al 7075. Because Eulerian beam bending equations do not predict extremely large deflections as well as FEA analysis, several tests were conducted to determine that the ratio of 3D to 2D FEA predicted stiffness values was approximately 12x, as expected from the Eulerian relations. Additionally, predicted peak stress was found to differ slightly between 2D and 3D analysis because of the assumptions made by planar simulations, but no general trend could be established as it was for stiffness. Based on past research from [19], 2D analysis of flexural hinges is valid if the out of plane depth to flexural beam thickness ratio is very small ($b/t < 2$) or very large ($b/t > 12.5$). Because the range of b/t ratios considered for this analysis are all >12.5, 2D analysis was

assumed to be useful for preliminary optimization work. All final models were still verified and checked with 3D analysis due to the complexity of the UEDPF mechanism. Figure 12 below shows the response surface's local sensitivity for the seven key UEDPF parameters identified by [11].

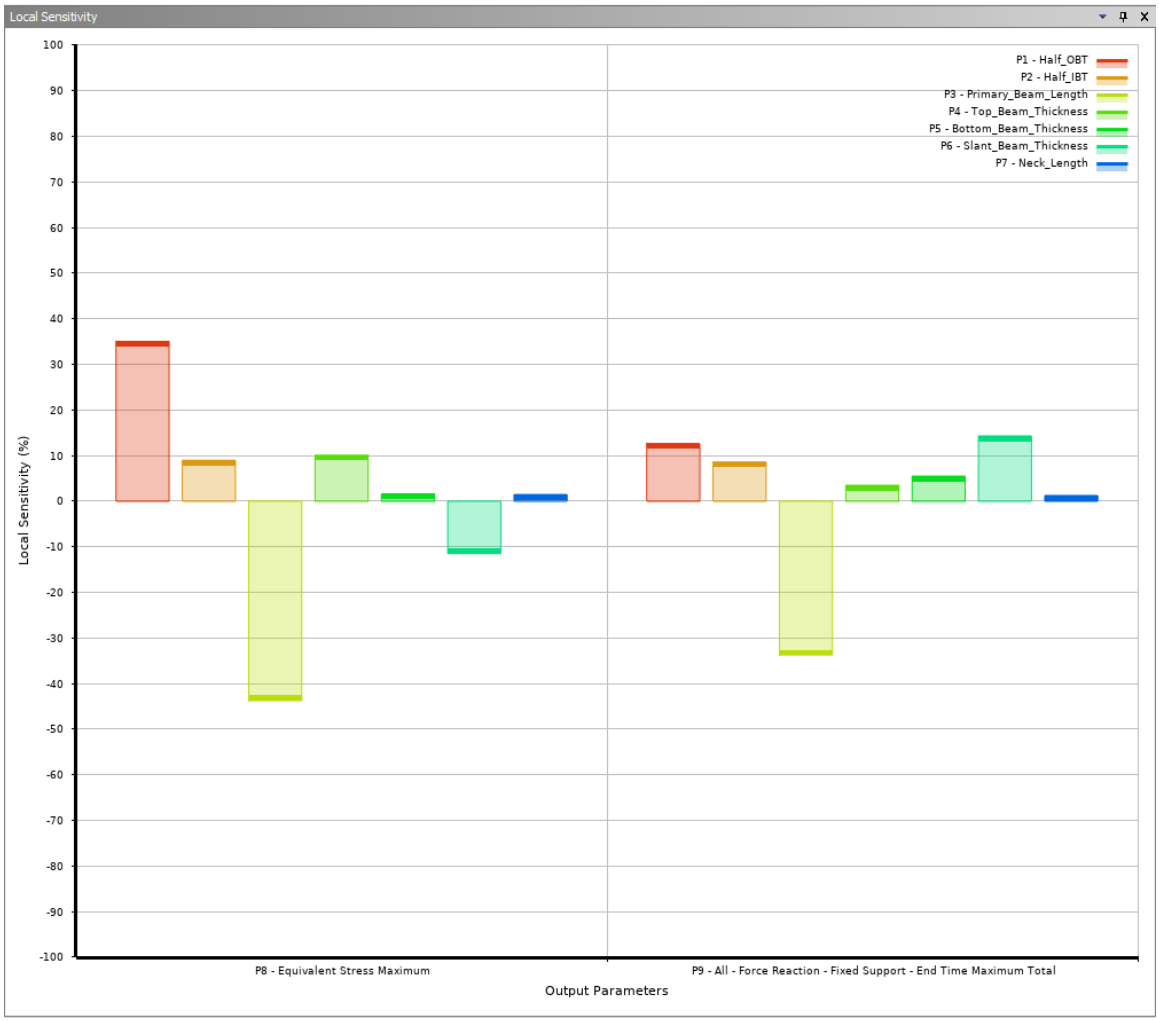

Figure 12: Sensitivity plot from optimization

The 2D FEA and response surface optimization steps were run iteratively until the response surface model achieved sufficient accuracy and the candidate points generated by

the optimization stopped changing significantly. Once this point of equilibrium had been reached, 3D analysis was used to verify the results from 2D simulations. Figure 13 below shows candidate points generated during the optimization process, plotted on axes of peak stress vs reaction force.

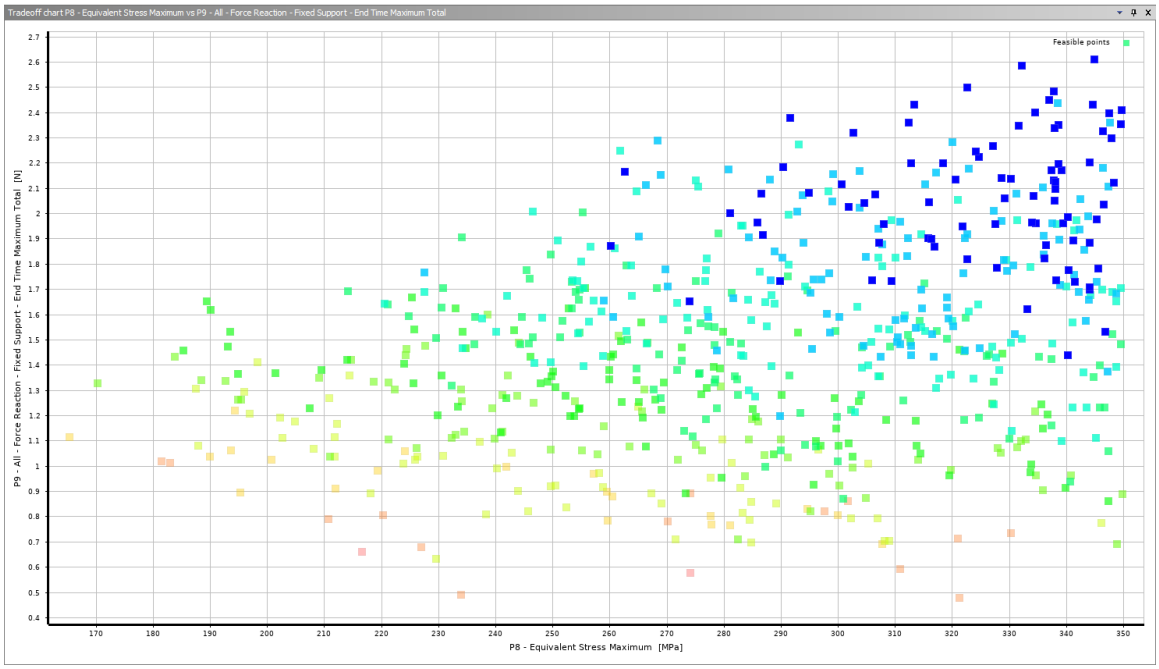

Figure 13: Plot of viable parameter sets generated from the optimization, on axes of the two output parameters

3.4) 3D QSA Simulations

The 3D FEA simulations of the QSAs which followed 2D FEA and optimization was the final step in the flexure optimization process before full stage verification simulations. Though this was the penultimate step in the design process, it was also intended to be the most accurate. Because large deflection compliant mechanisms exhibit significant elastic strains, FEA simulation requires an extremely fine mesh density to

produce useful and trustworthy results, limiting how large models can get [19]. Since the stage is constructed from four QSAs in a mirror symmetric format, all analysis for flexure failure can be done on a single QSA. Thus, the 3D FEA of QSAs were the most accurate models tested for the flexure design because a full stage 3D analysis required a drop in mesh size to be feasible to run with the computational resources at hand.

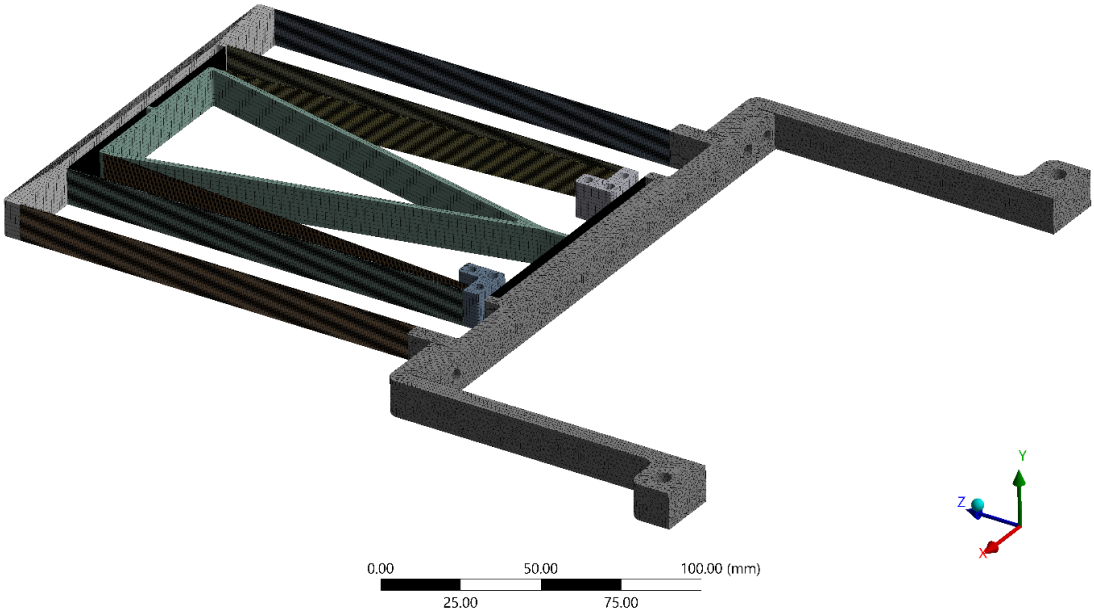

Figure 14: Mesh setup for 3D FEA simulations

The 3D FEA was set up with the same boundary conditions as the 2D FEA was, only the meshing method differed. The mesh chosen for 3D analysis was cartesian because it allowed a high degree of mesh control with hexahedral elements for maximum accuracy. Additionally, for finer mesh control and reduction of simulation time, the 3D body of the QSA was split into multiple bodies. Each flexure beam in the QSA was split into its own body and a fine mesh was applied, while the non-flexural parts of the UEDPF were meshed

in a coarser manner. A meshed model for 3D FEA is shown above in Figure 14. Contact mesh matching of the bodies was tested and a non-split QSA 3D FEA was performed to verify the validity of the split body model at predicting stress results. Symmetry was also employed to speed up the simulation runtime since the geometry is inherently symmetric about the midplane of the QSA. Figure 15 below shows the simulation setup for the 3D analysis, and Figure 16 shows an example result from a tested design point with similar stress distribution to the final chosen design.

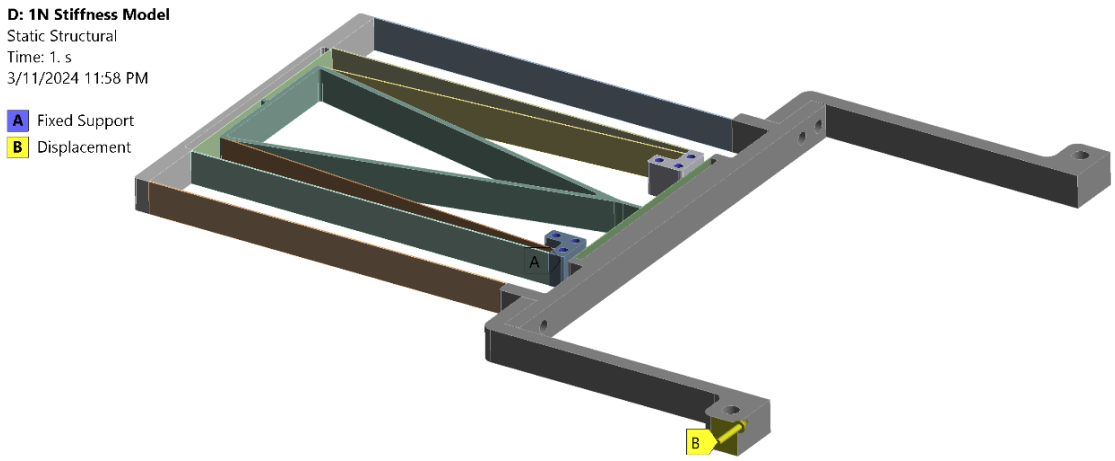

Figure 15: Setup of 3D FEA simulations

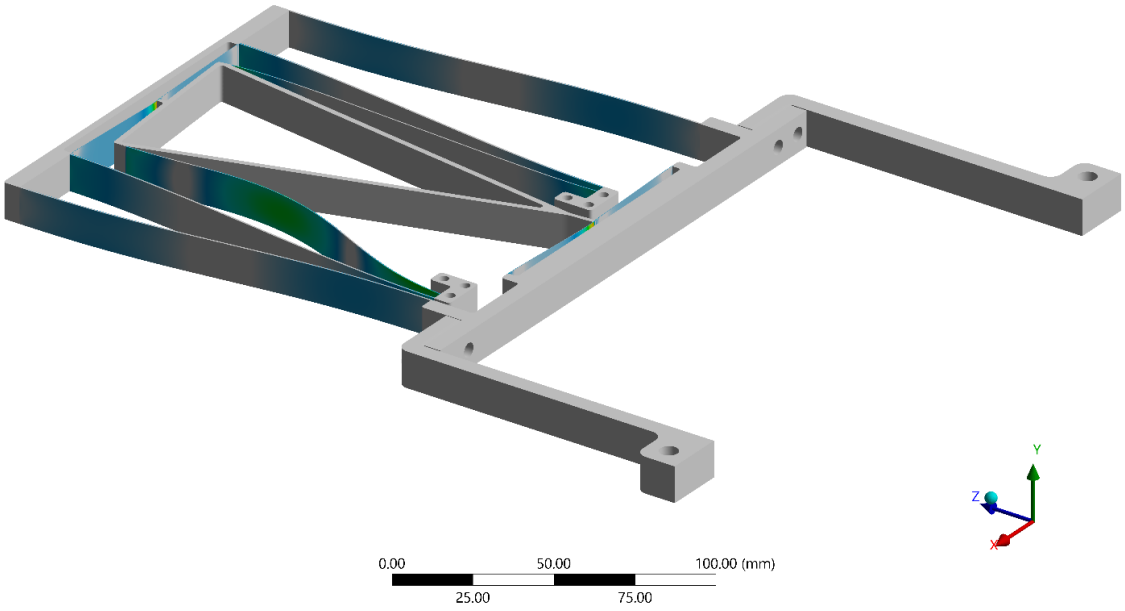

Figure 16: Example results from a 3D FEA

3.5) Full Stage 3D Simulations

After the individual 3D FEAs of QSAs verified the performance of the optimized flexure designs, the last step in the simulation process was to verify full stage 3D performance. The two simulations that were run for proposed optimized designs were a modal analysis and a 3D FEA of 2-axis max deflection. Due to the size of the full stage simulation, it was computationally inefficient to rely on 3D FEAs of the full stage to predict flexure failure, but a coarser mesh could be employed to verify that there was limited stress transfer between the two axis of the positioning stage and that all flexures would deform as predicted when placed in the full stage configuration.

The modal analysis run on the full stage model was used to evaluate relative performance differences between the baseline stage model and the new design. For

simulation efficiency, the QSAs were not split into as many bodies as previously for 3D FEA; they were split into the same number of bodies as they would be for manufacturing. Thus, for the new stage design, each UEDPF flexure was meshed as a single body. For the baseline stage design, each QSA was imported as a single body and meshed together since the stage had monolithically fabricated QSAs due to its smaller size [13]. Because the full stage is much larger than single QSAs, the mesh sizing had to be increased for simulation time to be kept within realistic bounds. Modal analysis is not as sensitive to mesh coarseness as structural FEA simulations are, so the results can be trusted as a comparison tool to evaluate relative performance increase over the baseline stage. The mesh chosen for the full stage simulations was a tetra method with an element size of 1mm and face refinement applied to the faces of the flexural beams. Figure 17 below shows the mesh used for the full stage analysis.

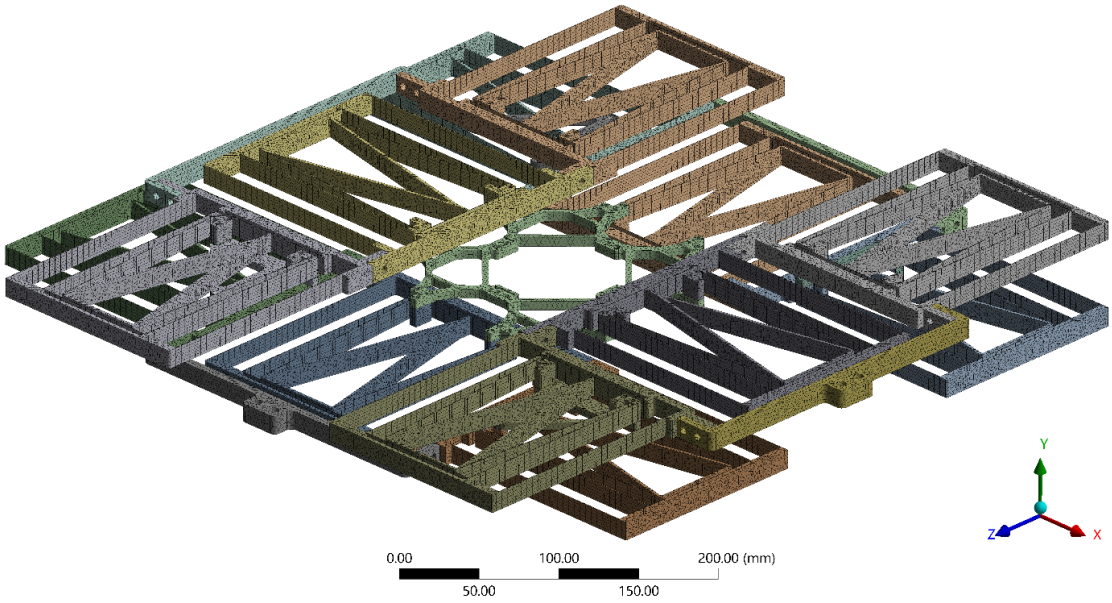

Figure 17: Mesh of full stage for modal analysis and final FEA

The final 3D simulation which was run on the full stage model was a fatigue analysis based on a structural FEA which simulated a 25mm deformation in both axes of the stage. Because fatigue life is affected by fabrication factors and the use of the stage, the chosen load for analysis was the maximum intended deformation of both axes of the stage since that represents the highest stress state that the stage as a whole would see during normal operation, and thus the results of the study should give a conservative estimate for fatigue life. Before the fatigue analysis was performed, a structural FEA was performed on the meshed model from the modal simulation to verify that further mesh refinement would not be required to produce stress values near those seen in the more accurate single QSA 3D simulations. Once the structural FEA verified that the stress values were near those seen in the finer-mesh single QSA simulations, a stress-life fatigue analysis was run

using the Gerber mean stress theory. The results from this analysis are discussed in the following section of this paper.

Chapter 4: Results, Conclusions, and Future Work

4.1) RESULTS

After multiple iterations, the optimization converged on a design and the resultant geometry was verified with FEA simulations. Table 3 below shows a comparison of the baseline stage's geometric parameters with the parameters of the new stage design.

Parameters	Baseline Design	New Stage Design
Outer Beam Thickness [mm]	0.2	0.608
Inner Beam Thickness [mm]	0.2	0.618
Primary Beam Length [mm]	101.85	147.75
Top Beam Thickness [mm]	0.2	0.205
Bottom Beam Thickness [mm]	0.2	0.294
Slant Beam Thickness [mm]	0.2	0.427
Neck Length [mm]	6.73	2.46

Table 3: Flexure geometric parameters for baseline stage and new design

As noted in Table 1, the performance of the positioning stage will be evaluated by its motion range, linear stiffness, natural frequency, life estimate, and planar footprint against the baseline stage developed by [13]. Table 4 below shows the performance of the newly designed stage relative to the baseline stage design for aforementioned criteria.

Evaluation Criteria	Target Value	Baseline Stage	New Stage Design
Motion range of stage center	50mm x 50mm	50mm x 50mm	50mm x 50mm
Linear stiffness of a single axis	1.44 N/mm maximum	0.46 N/mm	1.14 N/mm
First natural frequency modes of full stage	As high as possible with stiffness limitations	2.24 Hz	4.55 Hz
Fatigue life estimate	Greater than or equal to 10^9 cycles	$3.706 * 10^7$ cycles	$1.876 * 10^7$ cycles
Stage planar footprint	600mm x 600mm or smaller	445mm x 445mm	548.5mm x 548.5mm

Table 4: Performance of new stage design relative to baseline design

As can be seen in Table 4 above, the dynamic performance of the new stage design is improved over the baseline design in nearly all of the evaluation criteria. The baseline stage does outperform the new stage design is in fatigue life performance, but the difference between the predicted cycle life of the two stages is negligible for the use case of the uSLS printer. Table 5 below shows the first six resonance frequencies of the baseline stage compared with those of the new stage design. Figure 18 and Figure 19 below show the first six resonance frequencies of the baseline stage and new stage design, respectively.

	Baseline Stage	New Stage Design
Mode 1	2.24 Hz	4.55 Hz
Mode 2	2.24 Hz	4.55 Hz
Mode 3	55.75 Hz	46.46 Hz
Mode 4	64.68 Hz	50.38 Hz
Mode 5	67.79 Hz	51.72 Hz

Mode 6	68.42 Hz	55.89 Hz

Table 5: Resonance mode comparison between baseline stage and new stage design

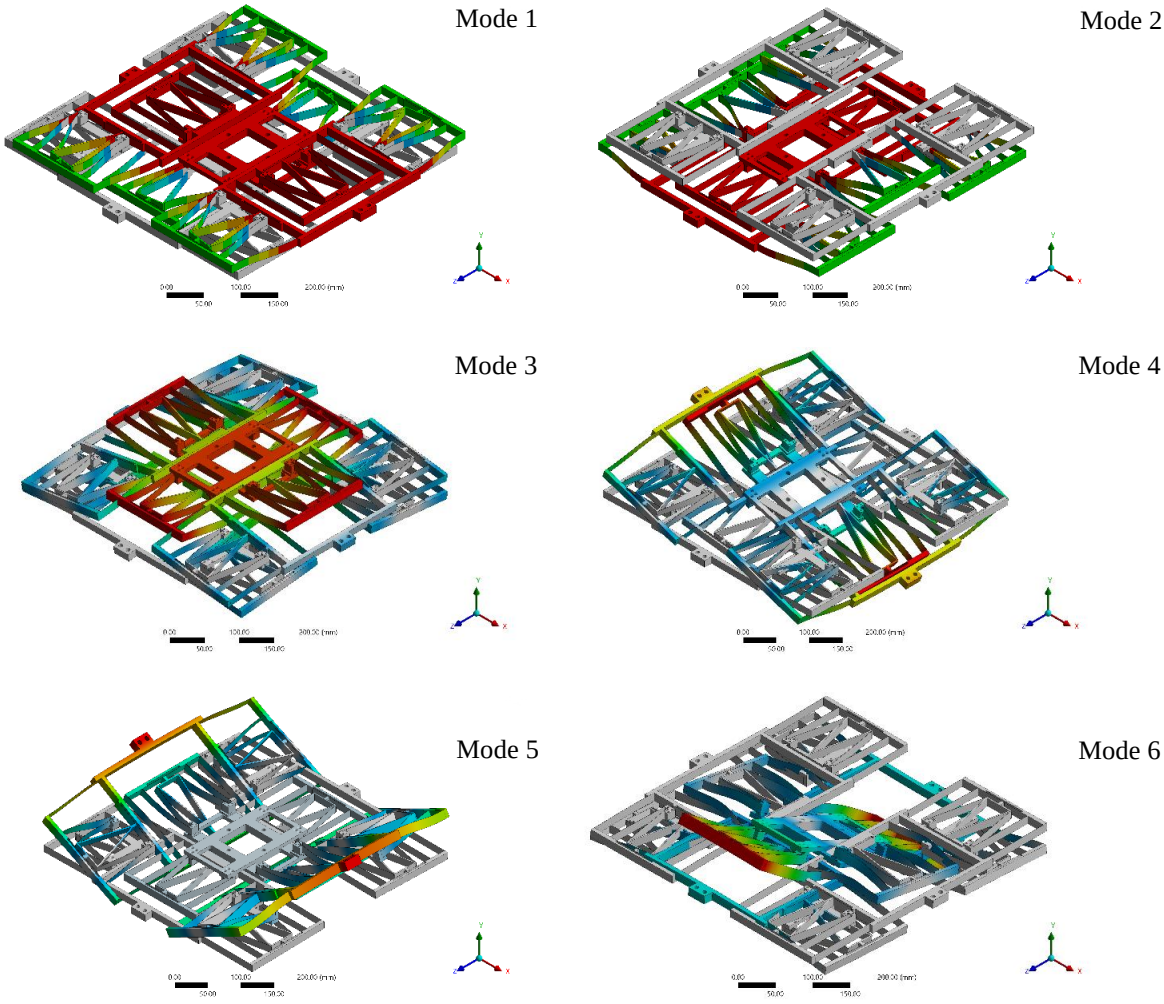

Figure 18: The first 6 resonance modes of the baseline stage

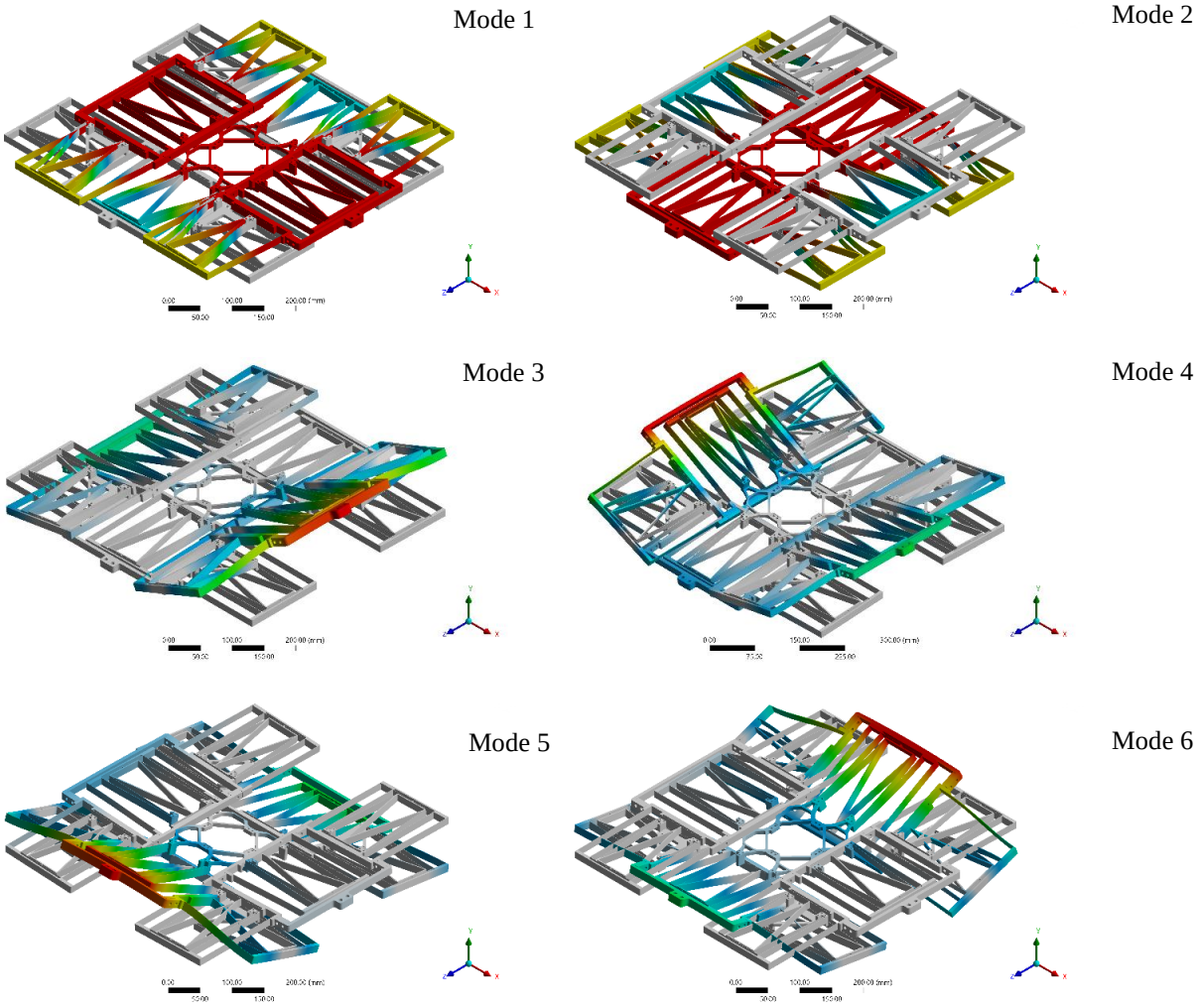

Figure 19: The first six resonance modes of the new stage design

4.2) CONCLUSIONS

The goal of this research was to redesign and optimize the nanopositioning stage for the uSLS printer designed by [13] in order to improve the dynamic performance of the stage and, in turn, the printer. This was accomplished through a multistage design and optimization strategy which consisted of three distinct parts: conceptual design, simulation & optimization, and final verification. In the conceptual design stage, the flexure for use

in the stage was chosen, the key parameters for optimization were identified, and the actuators were selected (which defined maximum flexure stiffness). The simulation & optimization step involved running batches of 2D FEA simulations to gather data, training a response surface based on the gathered data, running an optimization algorithm with the response surface to test thousands of flexures without needing to run time-consuming FEA simulations, and validating the results from the optimization to ensure fidelity. The final stage of the design process was to expand upon the candidate designs generated from the optimization and evaluate them with 3D FEA to characterize their performance against the baseline stage design from [13]. After the design process was completed, a new stage design has emerged which meets all design requirements, has superior dynamic performance to the baseline stage, and works within the existing architecture of the uSLS printer so actuators and structural components do not need to be changed to implement the new design.

4.3) FUTURE WORK

The work done in this project achieved favorable results, but there is room for improvement in future work. The following points detail ideas for future improvement, in order of broadest to most specific ideas.

1. The first further work which should be done with regards to this research is empirical testing. As of the time of writing, fabrication has begun on the stage model, but empirical testing has not yet occurred. The empirical tests should first aim to confirm FEA stiffness results, and, if any discrepancies are discovered, the

fabricated flexure's geometry and FEA model should be reviewed to confirm that no fabrication or modeling mistakes were made. After confirming deflection stiffnesses, the next step in the empirical testing process should be a white noise input which aims to test for the resonance modes of the stage. This will tell how accurate the findings from the modal analysis are and whether or not the model needs to be adapted to include the mass of the voice coil actuators in order to provide meaningful resonance mode predictions.

2. The broadest design improvement which could be implemented is the use of MCPFs instead of DPFs/UEDPFs. MCPFs present a significant size advantage and have shown to have promising dynamic results for shorter-stroke stages, so implementing the design methodology detailed in this paper for a MCPF-based stage design could potentially bring significant performance improvements. The first and largest challenge with a MCPF-based design would be attempting to integrate underconstraint elimination features within the multi-stage design as [11] did for the DPF.
3. Another implementation which could potentially result in a significant performance improvement for the nanopositioning stage is the inclusion of modal analysis in the earlier parts of the flexure optimization process. Though the modal responses of individual flexures do not directly dictate to the modal responses of the final stage, having individual flexures with better modal behavior would increase the resonance frequencies of the stage as a whole. If individual flexure dynamic performance

were considered during the optimization stage, stage performance could potentially increase.

4. The final suggestion for future work involves the UEDPF design. Though the underconstraint elimination feature is a breakthrough in the dynamic usability of the flexures, there are issues which crop up when using the design from [11] in a long-travel configuration. The top and bottom beams connect to the central triangle of the underconstraint elimination geometry through two vertical beams which are far stiffer than the top and bottom beams they connect to. The issue that arises during long travel of these flexures is the lack of compliance in those vertical beams causes the top and bottom beams to deflect more than they should, causing high stress concentrations around the connection point. If this geometry were altered slightly, the optimization could produce more favorable flexure designs since the current designs were limited by peak stress at the top and bottom beams, not in the main flexural beams.

References

[1] Akbarzadeh, M. B., Moeenfard, H., & Awtar, S. (2020). Nonlinear dynamic modeling of a parallelogram flexure. *Mechanism and Machine Theory*.

[2] Bai, R., Chen, G., & Awtar, S. (2021). Closed-form solution for nonlinear spatial deflections of strip flexures of large aspect ratio considering second order load-stiffening. *Mechanism and Machine Theory*.

[3] Ding, B., Li, X., Li, C., Li, Y., & Chen, S.-C. (2023). A survey on the mechanical design for piezo-actuated compliant micro-positioning stages. *Rev. Sci. Instrum. 94*.

[4] H2W Technologies. (2023, January). *Non-Comm DC Voice Coil Linear Actuator - NCC34-25-060-1X*. Retrieved from https://www.h2wtech.com/product/voice-coil-actuators/NCC34-25-060-1X

[5] Hao, G., He, X., & Awtar, S. (2019). Design and analytical model of a compact flexure mechanism for translational motion. *Mechanism and Machine Theory*.

[6] Heyman, I. (2022). *Design of a Magnetically-Levitated Long-Stroke 6-DOF Nanoprecision Positioning Stage.* Austin: The University of Texas at Austin.

[7] Howell, L. (2001). *Compliant Mechanisms.* New York: John Wiley & Sons Ltd.

[8] Kelly, J., Male, A., Rubies, N., Mahoney, D., Gomez-Gonzalez, M. A., Walker, J. M., . . . Quinn, P. D. (2022). The Delta Robot -- A long travel nano-positioning stage for scanning x-ray microscopy. *Rev. Sci. Instrum*.

[9] Lee, H.-J., Woo, S., Park, J., Jeong, J.-H., Kim, M., Ryu, J., . . . Choi, Y.-M. (2018). Compact compliant parallel XY nano-positioning stage with high dynamic performance, small crosstalk, and small yaw motion. *Microsyst Technol*, 2653-2662.

[10] Lyu, Z., & Xu, Q. (2023). Design and testing of a large-workspace XY compliant manipulator based on triple-stage parallelogram flexure. *Mechanism and Machine Theory*.

[11] Panas, R. M., & Hopkins, J. B. (2015). Eliminating Underconstraint in Double Parallelogram Flexure Mechanisms. *Journal of Mechanical Design*.

[12] Qin, Y., Shirinzadeh, B., Zhang, D., & Tian, Y. (2012). Compliance modeling and analysis of statically indeterminate symmetric flexure structures. *Precision Engineering 37*, 415-424.

[13] Roy, N. K., & Cullinan, M. A. (2018). Design and characterization of a two-axis, flexure-based nanopositioning stage with 50 mm travel and reduced higher order modes. *Precision Engineernig*, 236-247.

[14] Schitter, G., Åström, K. J., DeMartini, B. E., Thurner, P. J., Turner, K. L., & Hansma, P. K. (2007). Design and Modeling of a High-Speed AFM-Scanner. *IEEE Transactions on Controls Systems Technology*, 906-915.

[15] Thirumali Vasu, S. (2019). *Design and Computational Optimization of a Flexure-based XY Nano-positioning Stage.* Austin: The University of Texas at Austin.

[16] Xu, Q. (2016). *Design and Implementation of Large-Range Compliant Micropositioning Systems.* Fusionopolis: John Wiley & Sons Singapore Pte. Ltd.

[17] Xu, Q., & Wu, Z. (2018). Survey on Recent Designs of Compliant Micro-/Nano-Positioning Stages. *Actuators*, 1-20.

[18] Yong, Y. K., Moheimani, S. R., Kenton, B. J., & Leang, K. K. (2012). Invited Review Article: High-speed flexure-guided nanopositioning: Mechanical design and control issues. *Rev. Sci. Instrum*.

[19] Zettl, B., Szyszkowski, W., & Zhang, W. J. (2005). On Systematic Errors of Two-Dimensional Finite Element Modeling of Right Circular Planar Flexure Hinges. *Journal of Mechanical Design*, 782-787.

[20] Zhang, A., & Chen, G. (2013). A Comprehensive Elliptic Integral Solution to the Large Deflection Problems of Thin Beams in Compliant Mechanisms. *Journal of Mechanisms and Robotics*.

[21] Zhang, Z., Yan, P., & Hao, G. (2017). A Large Range Flexure-Based Servo System Supporting Precision Additive Manufacturing. *Engineering 3*, 708-715.